

Simulating Epileptic Seizures using the Bidomain Model

Jakob Schreiner (✉ jakob@xal.no)

Simula Research Laboratory

Kent-Andre Mardal

University of Oslo

Research Article

Keywords: Simulating Epileptic Seizures , Bidomain Model, synchronous neural activity

Posted Date: November 23rd, 2021

DOI: <https://doi.org/10.21203/rs.3.rs-1054431/v1>

License:   This work is licensed under a Creative Commons Attribution 4.0 International License.

[Read Full License](#)

Simulating Epileptic Seizures using the Bidomain model

Jakob Schreiner^{1,2,*} and Kent-Andre Mardal^{1,2,3}

¹Simula Research Laboratory, Oslo, 0164, Norway

²Expert Analytics AS, Oslo, 0179, Norway

³University of Oslo, Department of Mathematics, Oslo, 0851, Norway

*jakob@xal.no

ABSTRACT

Epileptic seizures are due to excessive and synchronous neural activity. Extensive modelling of seizures has been done on the neuronal level, but it remains a challenge to scale these models up to whole brain models. Measurements of the brain's activity over several spatiotemporal scales follow a power-law distribution in terms of frequency. During normal brain activity, the power-law exponent is often found to be around 2 for frequencies between a few Hz and up to 150 Hz, but is higher during seizures and for higher frequencies. The Bidomain model has been used with success in modelling the electrical activity of the heart, but has been explored far less in the context of the brain. This study extends previous models of epileptic seizures on the neuronal level to the whole brain using the Bidomain model. Our approach is evaluated in terms of power-law distributions. The electric potentials were simulated in 7 idealized 2D models and 3 MRI-derived 3D patient-specific models. Computed electric potentials were found to follow power-law distributions with slopes ranging from 2 to 5 for frequencies greater than 10 - 30 Hz.

1 Introduction

Epilepsy is the fourth largest neurological disorder with a prevalence of 7.1 per thousand in all ages¹. The condition involves seizures of abnormal brain activity, where waves of electrical activity propagate through the brain and cause a variety of symptoms, ranging from absent-mindedness to loss of consciousness. An epileptic seizure is due to excessive or synchronous neural activity in the brain^{2,3}. Extensive modeling has been performed on the neuronal level, but only few works^{4,5}, have to the authors' knowledge, scaled up the neuronal modelling to brain-wide simulations. The so-called Bidomain model, widely used for cardiac modeling, allows for this upscaling. Here, we investigate the simulation of seizures based on a specific neuronal model by Cressman et al.^{6,7} developed for epileptic seizures which is then combined with the Bidomain model.

To compare the computational model with actual seizures we have here chosen to quantify the simulation results in terms of the power-law distribution of the power spectral density measured at specific points, as the spectrum can be easily compared with EEGs and the power-law allows for quantification across several scales. Specifically, we will consider a power-law distribution of the form $p \sim f^{-\beta}$, where f is the frequency. Measurements of brain activity exhibit a $f^{-\beta}$ -like power spectrum at many spatiotemporal scales, see He⁸ for a review. During normal brain activity, the value of β is often found to be around 2⁹⁻¹⁴ for frequencies in the range 1 - 150 Hz, while the exponent is higher for higher frequencies¹⁵. Values between 0.5 and 3 have been explained in a theoretical and computational study¹⁶. In contrast, the neuronal model for seizures^{6,7} that is being considered here, displays power-law behaviour, with $\beta \approx 3.5$ but only in the range $f > 100$ Hz. Furthermore, Schreiner et al.¹⁷ have recently demonstrated that the power-law under ECT induced seizure, as measured with EEG, is in the range 3.4 - 4.2.

From a modelling point of view, the brain's behaviour during a seizure shares characteristics with the electrical activity of the heart. In a healthy heart, an electrical wave passes through the whole heart after originating at specific locations. In arrhythmia, however, the waves are chaotic and prevent the heart from a synchronous beat. The Bidomain model c.f. e.g.¹⁸⁻²² captures both the healthy case and arrhythmia and is, as such, a model that is capable of capturing complex electrical activity. In this paper, we will investigate whether the Bidomain model can be combined with a neuronal model for epileptic seizures, together with MRI-based geometries and diffusion parameters of the whole brain, to yield a plausible power-law distribution.

The Bidomain model has previously been used to simulate neuronal resting-state potentials during transcranial direct current stimulation⁵ and an ischemic region in a post-stroke patient^{23,24}. The Bidomain model includes the extracellular and the transmembrane potential, and couples naturally with dynamical models for the transmembrane potential. Bai et al.²⁵ simulated the electric field following direct current stimulation, representing the head as a passive volume conductor, but incorporating a Hodgkin-Huxley²⁶ type model in the cortical tissue. Their model captures neuronal activation, but not neuronal communication. There are other well-established models based on Poisson's equation describing electric currents in the different tissues in the brain, see e.g. Næss et al.²⁷ or Lee et al.²⁸. However, these models do not capture the temporal evolution of the electric field.

Model	Spatial dimension	Mesh	WM cell model	Anisotropy
<i>ODE</i>				
Model A	0	-	Cressman (stable)	-
Model B	0	-	Cressman (unstable)	-
<i>PDE & ODE</i>				
Model C	2	square	-	yes
Model D	2	square	Cressman (stable)	yes
Model E	3	Head	-	no
Model F	3	Head	-	yes
Model G	3	Head	Cressman (stable)	no

Table 1. A short summary of the models considered in this study. Models A and B are systems of ODEs describing cell membrane dynamics, and are coupled with the Bidomain model in the 2D models, C and D, as well as the 3D models, E, F, and G.

Alternative data-driven models have been developed for seizure dynamics, such as by Jirsa et al.²⁹, and extended to the whole brain using network models based on brain functional imaging³⁰.

Our task in this paper is to investigate whether macroscopic physics-based PDE models, such as the Bidomain model, combined with neuronal models for epileptic seizures give rise to plausible power spectra. Using the Bidomain model, we simulate the electric potential in the brain in an idealised 2D geometry and an MRI-based 3D geometry. Specifically, we utilize the neuronal model by Cressman et al.^{6,7} in which the excitability of the neurons is parametrized in terms of extracellular potassium in order to differentiate between seizures and normal activity. We will consider the importance of the geometry, the ODE-model, and the white matter (WM) anisotropy. To assess our approach we compare the power spectrum of the computed electric potential with the power-law behaviour of the EEG power spectrum.

2 Methods

We considered two different types of geometries: 1) an idealised 2D geometry, and 2), a patient-specific 3D geometry based on T1-weighted and diffusion weighted MR images, both illustrated in Figure 1. On these geometries the Bidomain model is coupled with neuronal models which are parametrized to either a seizure-like (unstable) or normal state (stable). An overview of the different models is provided in Table 1. Both model A and B are neuronal ODE models introduced in Cressman et al.^{6,7}, but Model B has high steady state extracellular potassium (K^+) concentration, $k_{0,\infty} = 8$ mM, compared to 4 mM in Model A. As such, Model B is in a seizure-like state, and alternates between periods of spike trains (bursts) and quiescence, seen in Figure 2. We compared models by counting the number of spikes, as also done in Erhardt et al.⁴, as well as computing the power-spectra.

Models C and D represent idealized 2D geometries, as shown in Figure 1a. The geometry is an idealisation of a cortical slice and measures 60 mm \times 40 mm. The grey matter (GM), cerebrospinal fluid (CSF), skull, and scalp each measures 4 mm across. We used this idealisation to study the effect of the tissue surrounding the brain, as well as the effect of an anisotropic conductivity tensor on the interaction between the Cressman model and the Bidomain model. The GM (dark grey) was modelled by the stable Cressmann model, Model A, except for the central red square in Figure 1a, which was modelled by the unstable Cressmann model, Model B. The WM (light grey) had an anisotropic conductivity tensor while the conductivity in the GM, CSF, skull and scalp was isotropic. We considered two variations of this model, one with no cell model in the WM, termed Model C, and one with Model A in the WM, termed Model D. In the 2D models, the GM and WM was further distinguished by the isotropic conductivity in the GM and anisotropic conductivity in the WM. The anisotropic conductivity tensor in the WM of the 2D models was

$$\begin{pmatrix} \sigma_t & 0 \\ 0 & \sigma_l \end{pmatrix}, \quad (1)$$

where $\sigma_l = 10\sigma_t$ and $\sigma_t = 0.1$, that is, the principal component of the conductivity tensor was oriented vertically. In the right part of the WM, σ_l and σ_t in Equation 1 are swapped, i.e., the conductivity tensor is oriented horizontally.

The three patient-specific 3D models (Models E, F, G) were based on surfaces of the pia, WM, and ventricles. The surfaces were reconstructed from a MRI of a human head using FreeSurfer^{31,32}. We represented the subarachnoid space (SAS) by the convex hull of the pia expanded 3mm along the outward facing normal vector. The skull and scalp were similarly defined as the expanded convex hull of the SAS and skull respectively. The resulting mesh is shown in Figure 1b, and has 72 million cells. Volume meshes were created with SVMTK³³, which is based on CGAL³⁴. As in the 2D models, the GM is modelled by Model

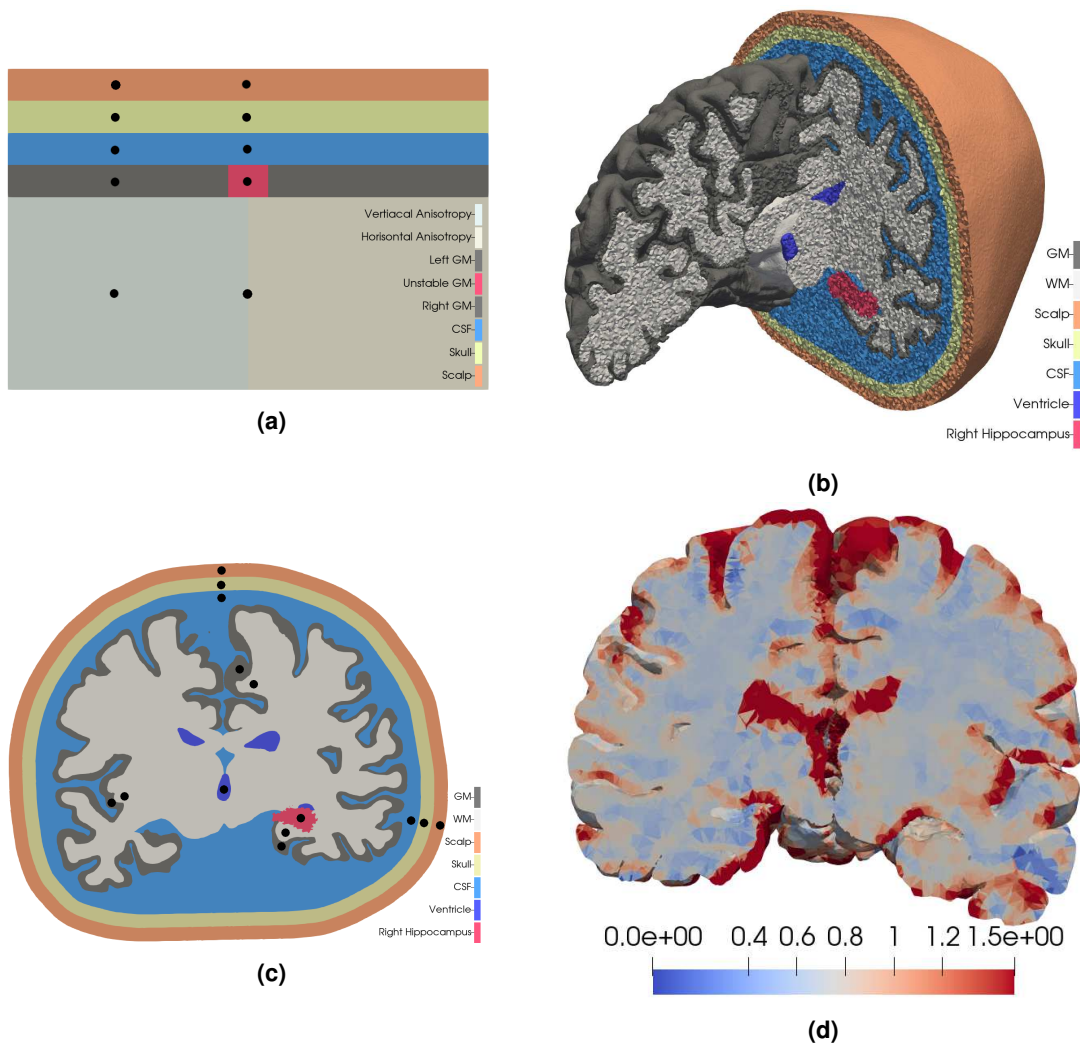


Figure 1. Computational geometries (a) An idealised 2D model of a slice of the head with, from the top, scalp (orange), skull (yellow), cerebrospinal fluid (blue), grey matter (dark grey and red), and white matter (two shades of light grey). The central GM (red) is modelled by an unstable neuronal model, Model B, while the rest of the grey matter (dark grey) is modelled by a stable neuronal model, model A. The conductivity is isotropic, except in the white matter. The anisotropic conductivity tensor in the white matter is oriented vertically in the left part and horizontally in the right part. The simulated electric potential is measured at locations marked by black dots (b) The 3D patient specific head model. The colours are the same as in (a), however, the ventricles are marked dark blue, and the right hippocampus is marked in red. As in (a), the grey matter is modelled by Model A, while the right hippocampus is modelled by Model B. (c) A slice of the head model in (b). The simulated electric potential is measured at locations marked by the black dots. (d) The mean diffusivity is highest in the ventricles and the CSF, both showing up in red. The mean diffusivity is $1/3 \text{Tr}(M)$, where M is the conductivity tensor. The conductivities are measured in mS/cm.

A, except for the right hippocampus, which is modelled by model B. Model E has isotropic WM conductivity and no WM cell model. Model F has an anisotropic conductivity tensor in the WM, and no WM cell model. The conductivity tensor was assumed proportional to the water diffusion tensor^{35,36}, which was constructed from the diffusion tensor imaging (DTI) using FreeSurfer. That is, we have followed Tuch et al. in quantitatively estimating the anisotropic conductivity tensor from water diffusion in the brain³⁵, an approach validated in the study by Bangera et al.³⁶. The approach used by Bangera et al. assumes that the scaling between the diffusion tensor and the conductivity tensor is the same throughout the brain. The mean diffusivity of the conductivity tensor is shown in Figure 1d. Model G has isotropic WM conductivity and Model A as a WM cell model. Experiments with model G were also run with a Morris-Lecar model³⁷ in the WM, rather than Model A. The small black circles in Figures 1a and 1c show locations where time traces of the potential were sampled. The power spectral density (PSD) of the

	Value	Units
Membrane capacitance (C_m)	1	μF
Cell membrane surface per unit volume (χ)	1.26×10^3	1/cm
Tissue type	Conductivity Intracellular	mS/cm Extracellular
Grey matter	1	2.78
White matter	1	1.26
CSF	10^{-4}	17
Skull	10^{-4}	0.1
Skin	10^{-4}	4.3

Table 2. Physical parameters

electric fields were estimated using Welch’s method³⁸ implemented in *scipy* version 1.6.1³⁹.

The approval for MRI-observations was retrieved by the Regional Committee for Medical and Health Research Ethics (REK) of Health Region South-East, Norway (2018/1093). The study participants were included after written and oral informed consent. All methods were performed in accordance with the relevant guidelines and regulations.

Following²², the Bidomain model reads

$$\begin{aligned} \nabla \cdot (M_i \nabla v) + \nabla \cdot (M_i \nabla u_e) &= \chi C_m \frac{\partial v}{\partial t} + \chi I_{ion} \\ \nabla \cdot (M_i \nabla v) + \nabla \cdot ((M_i + M_e) \nabla u_e) &= 0, \end{aligned} \quad (2)$$

with the boundary conditions

$$\begin{aligned} (M_i \nabla v + M_i \nabla u_e) \cdot \mathbf{n} &= 0 \\ (M_e \nabla u_e) \cdot \mathbf{n} &= 0. \end{aligned} \quad (3)$$

Here, v and u_e are the transmembrane and extracellular potential respectively, and M_i and M_e are the intracellular and extracellular conductivity respectively. Furthermore, C_m is the cell membrane capacitance and χ is the membrane surface area per unit volume. The ionic current across the cell membrane, I_{ion} , is modelled by the Cressmann model. In the CSF, skull and scalp M_i is 4 orders of magnitude less than M_e in the GM and WM. Table 2 provides an overview of physical parameters used in this study. Values for C_m , χ , and GM and GM conductivities are taken from Dougherty et al⁵, while CSF, skull and scalp conductivities are taken from Vorwerk et al.⁴⁰.

The Bidomain model coupled with the Cressman model was solved with a second order splitting scheme in time, see²² for a derivation, and a time step of 0.025 ms. The ODE model was solved only in the GM unless specified otherwise, using the forward Euler method. In space, Equation 2 was discretised with the finite element method using first order continuous Lagrange elements. The linear system was solved using the generalised minimal residual method (GMRES) preconditioned with an algebraic multigrid method with relative tolerance set to 10^{-5} and absolute tolerance set to 10^{-50} . The software used to solve the equations is based on *cbcbeat*⁴¹ built around the FEniCS project version 2019.1.0^{42,43}.

3 Results

The stable Cressman model, Model A, spiked 5 times, then remained quiet, and did not exhibit any bursts. In contrast, during the 10 second simulation the unstable Cressman model, Model B, spiked 241 times in 5.7s, then entered a period of quiescence, see Figure 2e. It continues to alternate between bursts and periods of quiescence. This is similar to what was observed in the study by Erhardt et al.⁴.

In the idealized 2D models, waves originate in the central unstable region and spread along the GM in both the model with and without a WM cell model, Model C and Model D, respectively, see Figures 3a and 3c. To count the spikes, the potential was measured in the locations indicated in Figure 1a and adjusted accordingly as the thickness of the CSF, skull, and scalp was changed. There were 135 identifiable spikes in the initial burst in the Model C lasting 3.1 seconds, as such the burst duration is shorter in Model C, but the number of spikes per second is roughly similar to Model B. Model D spiked continuously during the 10 second simulation, with no identifiable bursts, counting 1873 spikes. Furthermore, the magnitude of the spikes were approximately doubled and the spike frequency was increased by a factor 4.3 compared to Model C. As such, it appears that the

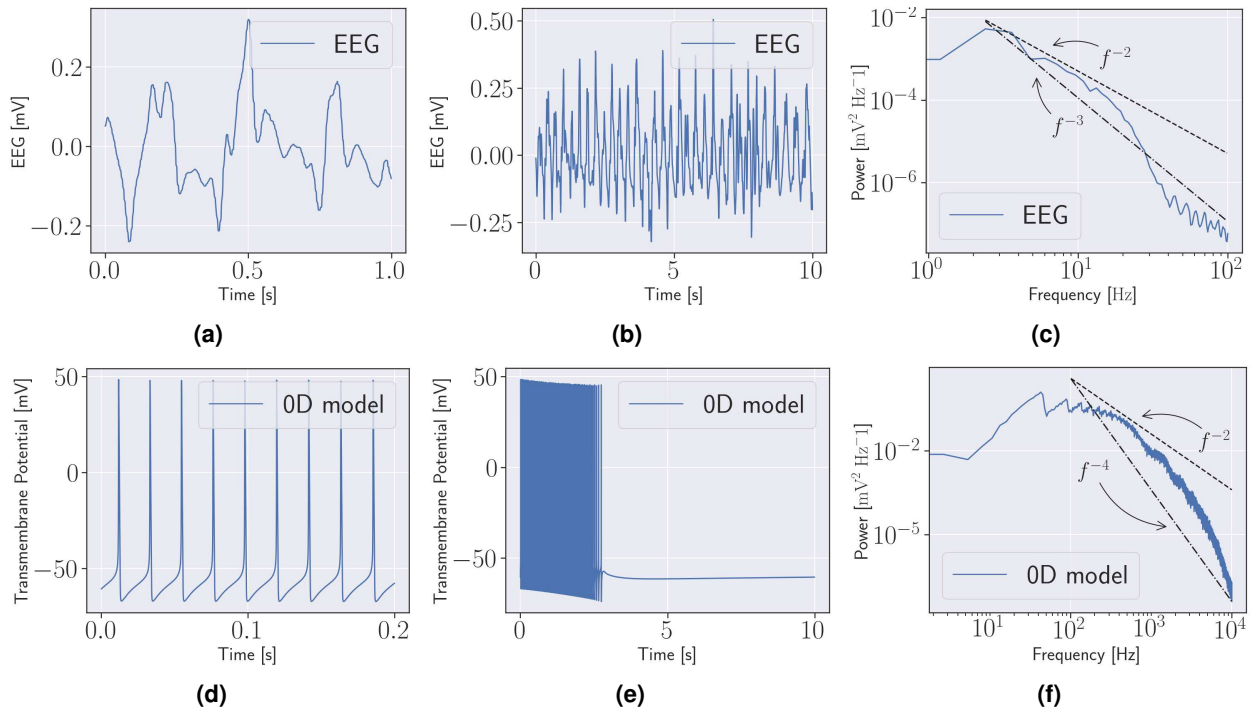


Figure 2. EEG and cell model The top row show an EEG from a patient experiencing a seizure. (a) shows one second of the EEG, (b) shows 10 seconds, and (c) the power spectrum computed from the 10 second segment in (b). The bottom row shows the simulated transmembrane potential from model B. (a) shows 0.2 seconds, (b) 10 seconds with an initial period of spikes, a burst, followed by a period of quiescence, (c) the power spectrum computed from the burst in (b).

coupling represented by the Bidomain model may both accelerate and decelerate the neuronal firing, depending on the WM model. Finally, the Bidomain model enable spreading from an unstable domain to the complete domain, even though the bulk of the domain is initialized by stable parameters of the Cressman model, i.e. extracellular potassium of 4 mM.

The effect of the mesh resolution was investigated in detail in 2D. The number of spikes during the 10 second simulation of Model C is listed in Table 3 and demonstrate that a mesh with 1738 cells adequately resolves the travelling waves, see Figure 3a. For coarser meshes the waves failed to propagate. The 1738 mesh had 5 cells across the GM. The resolution was higher in the GM than in the CSF. In the simulations with a cell model in the WM, the resolution in the GM and WM was the same.

# cells	# spikes
6120	135
1738	135
514	132 (3)

Table 3. The number of spikes and the number of cells in 2D simulations in the domain in Figure 1a. The spikes were counted throughout the GM. Only in the coarsest case did any waves fail to propagate from the unstable region. In that case, only the first three (i parenthesis) spread to the stable parts of the GM. The total number of spikes were counted over a 10 second interval.

The effect of the anisotropic conductivity tensor in Model C was evident in the magnitude of the extracellular potential. That is, the passing waves in the GM propagate further into the WM see Figure 3a. In detail, in the left part, where the conductivity tensor is oriented vertically, the extracellular potential is affected along the complete WM column of 24 mm. In the right part, where the conductivity tensor is oriented horizontally, the corresponding propagation is only 2-3 mm. In Model D, the 2D model with a WM cell model, the effect of the anisotropic conductivity tensor is evident in the deflection of the waves in the WM, as seen in Figure 3c. In both Model C and D, the orientation of the conductivity tensor affects the magnitude of the extracellular potential, and as such, the magnitude of the PSD, but not the power-law exponent.

To investigate the sensitivity of the thickness of the CSF, skull, and scalp on Model C, we performed two new simulations increasing and decreasing the thickness of the CSF, skull, and scalp by a factor of 1/3. Similarly, investigating the sensitivity

to the anisotropic conductivity tensor, we ran four new experiments independently increasing and decreasing σ_l and σ_t by a factor of 1/3. As such, the variation in CSF, skull, and scalp thickness and anisotropy accounts for 7 different simulations. The variations to the thickness of the CSF, skull, and scalp as well as the individual components of the conductivity tensor resulted in minor variations in the magnitude of the PSD, seen in Figure 3b. Here, notice that for each colour there are 7 lines representing the different simulations. We also remark that the changes in the potential due to these variations are smaller than the differences in the potential between the compartment (WM, CSF, skull, scalp). The PSD in the GM was unaffected by these perturbations.

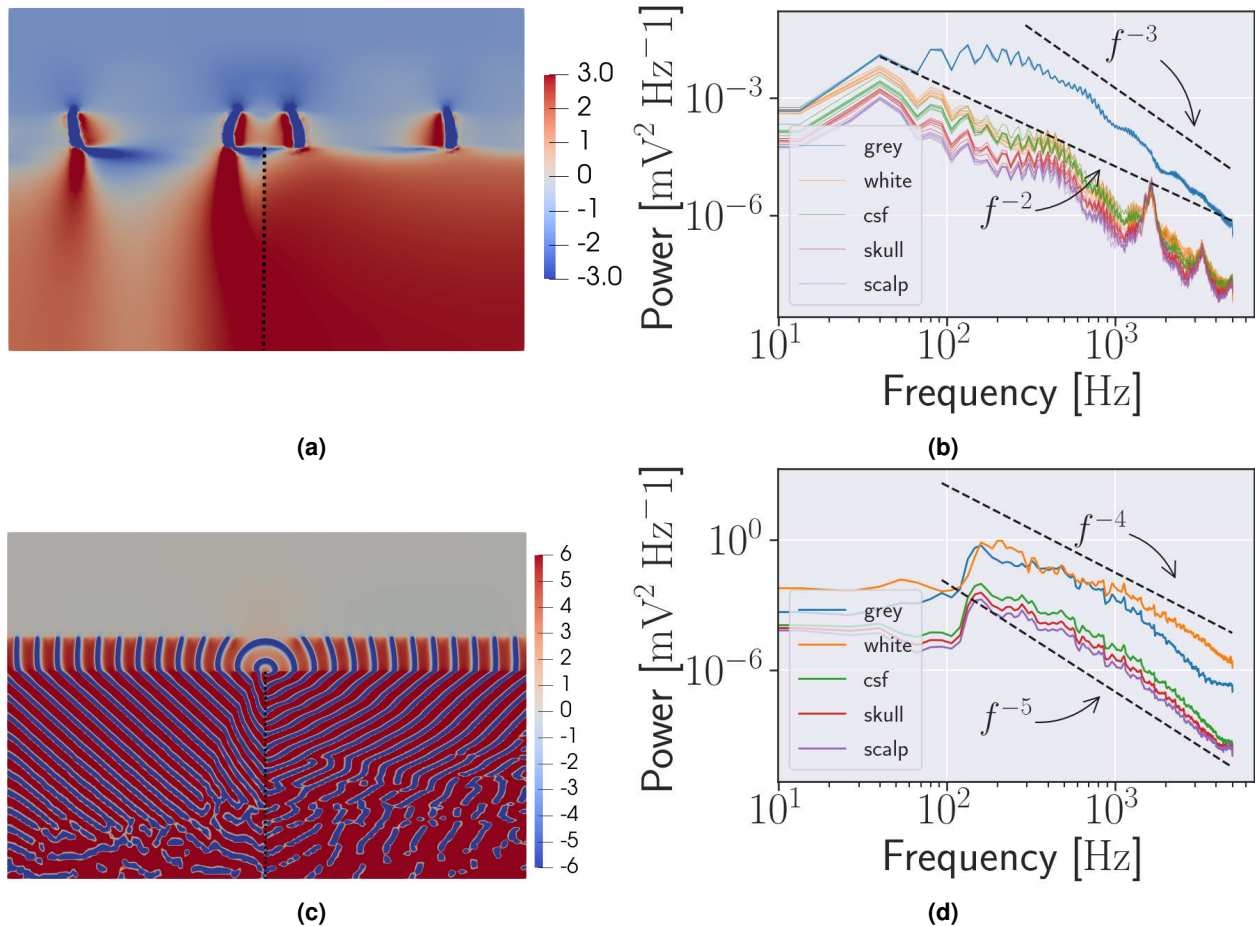


Figure 3. 2D simulations and power spectra (a) A snapshot of the simulated extracellular potential in Model C. The waves spread through the GM from the central unstable region. (b) The extracellular potential in the central (unstable) GM. Variations to the thickness of the CSF, skull and scalp as well as the individual components of the conductivity tensor by a factor of 1/3 affect the magnitude of the PSD in the WM, GM, CSF and skull, but not the GM. Each variation is represented by a thin line. (c) A snapshot of the simulated extracellular potential in Model D. Waves spread from the GM from the unstable central region, and also into the white matter. (d) The PSD of the extracellular potential in the different tissues with no cell model in the WM.

The geometry of the 3D model is shown in Figure 1b and the measurement locations are shown in Figure 1c. The mesh contained 72 million finite element cells and the resolution was similar to the idealized, resolved 2D geometry in the sense that there were 5 cells across the GM. The individual cells can be seen in the slices. In 3D, waves spread from the destabilised hippocampus, and through the surrounding GM in the model with an isotropic conductivity tensor, Model E, and the model with an anisotropic conductivity tensor, as seen in Figure 4 after 100 ms. In the hippocampus, the extracellular voltage traces were similar to Model B. There were between 10 and 13 spikes in the hippocampus during the 100 ms of the simulation of model E and F, see Figure 5a, depending on the exact measurement location. That is, the number of spikes per second is between 100 and 130, which is more than twice as high as in the idealized 2D model without WM model, Model C. The anisotropic conductivity tensor in Model F did not affect the frequencies in the WM or the GM, but the magnitude of the extracellular potential was greater throughout the brain, as seen in Figure 5b. In Model G, the model with a stable Cressman model in WM, there were no spiking in the hippocampus. With a Morris-Lecar model³⁷, the number of spikes were the same as models E and

F.

The β -parameter of the power-law of the power spectrum of Model B, see Figure 2f, was between 2 and 3 for f between 100 and 5000 Hz. The PSD of the extracellular potential of Model C followed a power-law with $\beta \approx 2$ for f between 40 Hz and 5000 Hz in the WM, and $\beta \approx 3$ for f between 300 Hz and 5000 Hz in the GM, see Figure 3b. The PSD of the extracellular potential in Model D followed a power-law with an exponent close to 5 in the "passive" tissue, the skull, scalp, and CSF, and 4 in the "active" tissue, the GM and WM. Both power-laws are for f between 150 Hz and 5000 Hz, see Figure 3d.

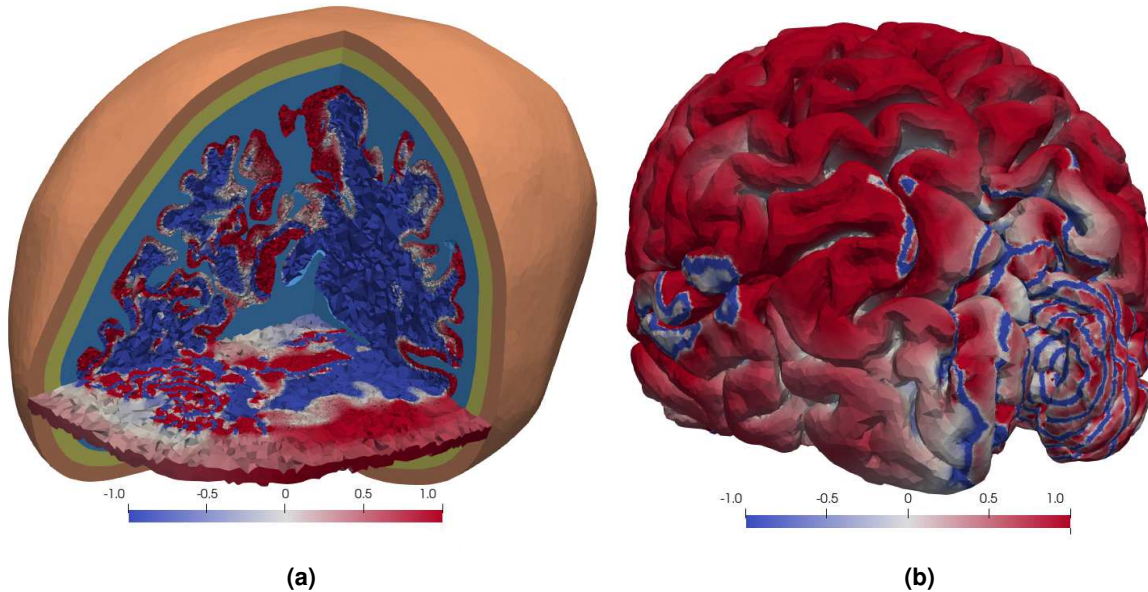


Figure 4. 3D simulations Two visualisations of the extracellular potential in the head and on the brain surface after 100 ms. The colormap is chosen to highlight the waves. (a) The extracellular potential throughout the brain and the surrounding tissue in a corner of the head. The surrounding tissue is shown in colors similar to Figure 1b, while the magnitude of the extracellular potential shown is shown in the GM and WM. The horizontal slice also shown the magnitude of the extracellular potential in the CSF, skull and scalp. (b) The extracellular potential on the surface of the brain.

The power-spectra of Model E and Model F were identical in the hippocampus, and is shown in Figure 5c. The peak of the PSD was at 300 Hz. The two black lines show a power-law corresponding to $\beta = 2$ and $\beta = 3$ for f between 100 and 5000 Hz. The power-law in the WM in the model with an isotropic conductivity tensor, Model E, and anisotropic conductivity tensor, Model F, is shown in Figure 5d, with a peak located at 10 Hz. The two black lines illustrate power-laws with slopes $\beta = 3$ and $\beta = 2$ for f between 10 and 5000 Hz.

4 Discussion

In this paper we simulated the electrical potential in a human brain during a seizure using the Bidomain model with a Cressman^{6,7} excitation model in 10 geometries (7 idealized 2D models and 3 MR based 3D models). The Bidomain-Cressman model resulted in electrical waves propagating through the brain from unstable to stable regions as also observed in Erhardt et al.⁴. The PSD of these waves follow a power-law distribution similar to what is found in EEGs. That is, the power-law slopes during a seizure have values from 2 to 5, depending on the model. In detail, for all models that did not have an active model in WM the slope was found to be between 2 and 3, while for the idealized model with a stable Cressman model in the WM a slope of between 4 and 5 was observed. The values are in agreement with previous studies^{9-15,44-46}, where values between 2 and 4 are reported, although none of these studies investigate seizures in humans. Observed power-law slope in EEG was recently reported to be between 3.4 and 4.2¹⁷ during ECT-induced seizures. We remark that it is interesting to observe that the Bidomain model extended the slope of the power-law in the Cressman model from 100 - 5000 Hz down to around 30 Hz. In EEGs, frequencies from a few Hz to a few hundred Hz are commonly measured, and as such the Bidomain model brings the models into the regime of interesting frequencies.

The anisotropic conductivity tensor did not have a significant effect on the distribution of power in the PSD in any of the models, as compared with the isotropic conductivity. However, the anisotropy has a significant effect on the magnitude of the extracellular potential. In this study we have used physiologically realistic values from the literature⁵, although the context was

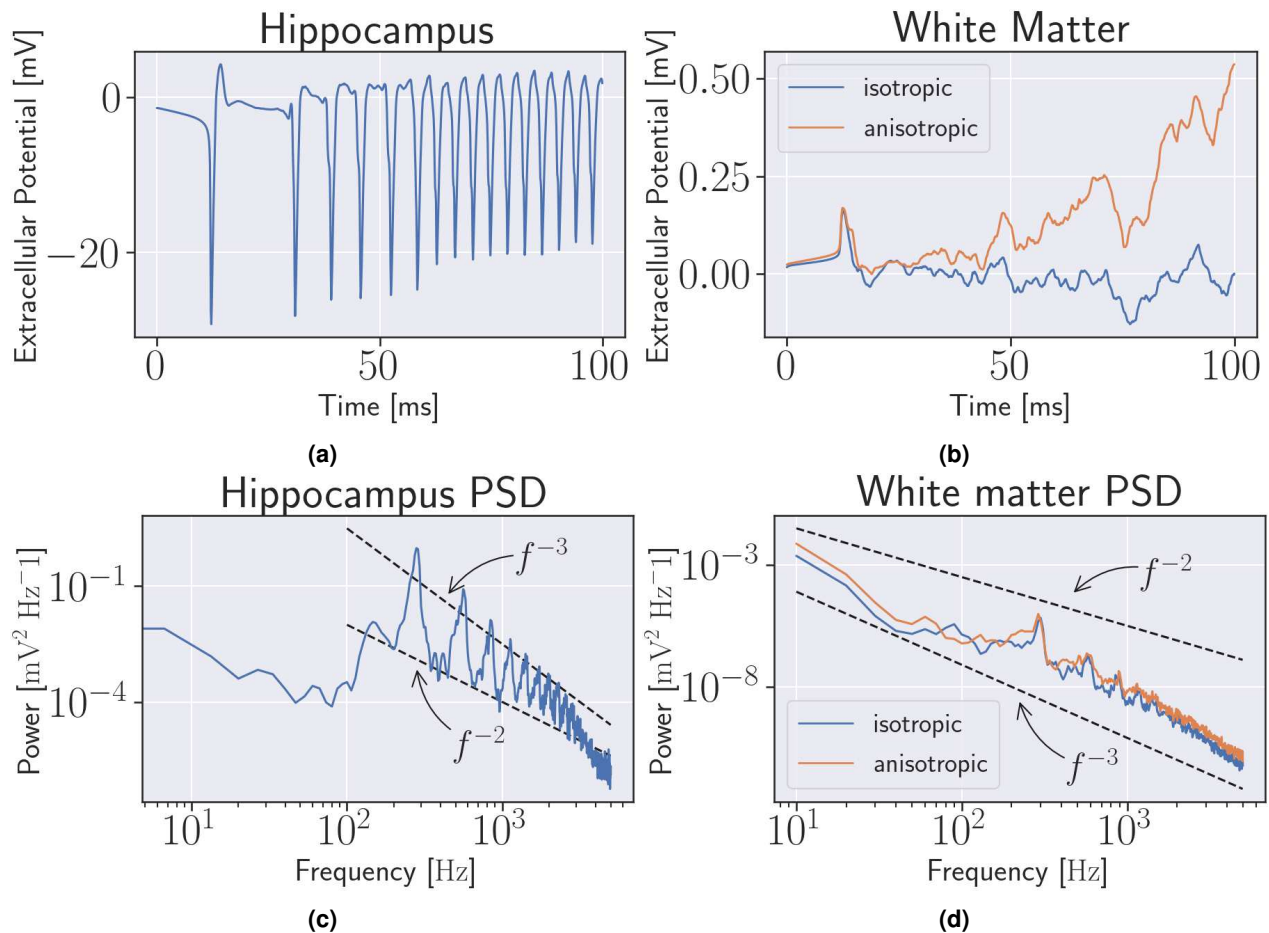


Figure 5. 3D spikes and power spectra (a) The simulated extracellular potential in the right hippocampus in Model E. (b) The extracellular potential in the WM in the left hemisphere from Model E and Model F. (c) The power spectrum of the potential in (a). (d) The power spectrum of the potential in (b).

here isotropic. Previous studies have found that tissue anisotropy affects electric field magnitudes^{28,36}, but we are unaware of studies investigating the effect on frequency content.

The Bidomain model assumes a purely resistive medium²², and the possibly frequency dependent properties of the extracellular medium may limit the applicability of the Bidomain model. According to Nunez and Srinivasan, typical EEG frequencies less than 100 Hz are not affected by capacitative effects of the extracellular medium⁴⁷. Furthermore, the resistive properties of the extracellular medium have been reported to be independent of the frequency⁴⁸ or weakly frequency dependent⁴⁹. More recent studies, however, suggest that there may be important frequency dependencies of the extracellular medium. Gomes et al. found a strong frequency dependence in the extracellular conductivity⁵⁰, linking the frequency dependence to ionic diffusion. A possible explanation of the discrepancies lies in the measurement technique, and the findings are controversial, see the discussion^{51,52} following the study by Gomes et al.⁵⁰. Assuming ionic diffusion is the origin of the frequency dependence in the extracellular conductivity, Bédard and Destexhe show that this could explain the origin of the power-law scaling in the local field potential⁵³. In the Bidomain model in the current study, a quasi-static assumption is used to derive the equations solely in terms of the electric potential of the intra and extracellular electric fields, but this assumption can only be made if the medium is frequency independent.

The neuronal model by Cressman et al.^{6,7} is developed to model the activity of one neuron. The model has been further developed in Wei et al.⁵⁴ to incorporate chloride ion and oxygen concentrations. This extended model exhibit a broader range of neuronal activities such as seizures caused by hypoxia or cortical spreading depression. In contrast, an EEG is measured with electrodes placed on the scalp and represents an average of electrical activity within the brain. As such, the electric potential at a specific location of the skull is generated by the activity of neurons numbering in the tens of millions⁴⁷. Our results here indicate that the Bidomain model has the potential to bridge the gap between these two scales in certain applications.

We have investigated the effect of a WM cell model in both 2D and 3D simulations. While using the stable Cressman

model in the WM had a significant effect on burst duration, power-law slope and frequency range in 2D, the corresponding simulation in 3D demonstrated that the unstable hippocampus was prevented by the WM from spiking. A further experiment with a Morris-Lecar model³⁷ in the WM in a 3D simulation had negligible effect in the simulated potentials when compared with no WM cell model. A previous study of the coupling of the Cressman and Bidomain models showed that there is a balance between the conductivity and the size of the unstable region, i.e., the right hippocampus⁴. If the conductivity is too high, or the unstable region too small, the stable regions of the model dominates and spiking stops. This issue has not been addressed in the 3D models due to the computational costs. Compared to the 100 billion neurons and equal number of glia in the brain⁵⁵, our realistic head models consist of 70 million cells. The 3D simulations of 100 ms of the brain activity took 200 hours with 16 cores using 16 GB of memory each.

5 Conclusion

This study shows that the Bidomain model gives rise to plausible power-spectra in the extracellular potential in idealised and realistic models of the brain. Neither an anisotropic conductivity tensor, nor varying the thickness of the CSF, skull, or scalp had any discernible effect on power-law distribution in the PSDs in any of the models. The WM cell model has a profound effect on the power spectra in 2D, but not in 3D, in the current study.

6 Data Availability

Meshes used on this study are available from the corresponding author upon request.

References

1. Hirtz, D. *et al.* How common are the common neurologic disorders? *Neurology* **68**, 326–337 (2007).
2. Fisher, R. S. *et al.* ILAE official report: a practical clinical definition of epilepsy. *Epilepsia* **55**, 475–482 (2014).
3. Gotman, J. A few thoughts on what is a seizure?. *Epilepsy & Behav.* **22**, S2–S3 (2011).
4. Erhardt, A. H., Mardal, K.-A. & Schreiner, J. E. Dynamics of a neuron–glia system: the occurrence of seizures and the influence of electroconvulsive stimuli: A mathematical and numerical study. *J. computational neuroscience* **48**, 229 (2020).
5. Dougherty, E. T., Turner, J. C. & Vogel, F. Multiscale coupling of transcranial direct current stimulation to neuron electrodynamics: modeling the influence of the transcranial electric field on neuronal depolarization. *Comput. mathematical methods medicine* **2014** (2014).
6. Cressman, J. R., Ullah, G., Ziburkus, J., Schiff, S. J. & Barreto, E. The influence of sodium and potassium dynamics on excitability, seizures, and the stability of persistent states: I. single neuron dynamics. *J. computational neuroscience* **26**, 159–170 (2009).
7. Ullah, G., Cressman Jr, J. R., Barreto, E. & Schiff, S. J. The influence of sodium and potassium dynamics on excitability, seizures, and the stability of persistent states: II. network and glial dynamics. *J. computational neuroscience* **26**, 171–183 (2009).
8. He, B. J. Scale-free brain activity: past, present, and future. *Trends cognitive sciences* **18**, 480–487 (2014).
9. Beggs, J. M. & Plenz, D. Neuronal avalanches in neocortical circuits. *J. neuroscience* **23**, 11167–11177 (2003).
10. Beggs, J. M. & Plenz, D. Neuronal avalanches are diverse and precise activity patterns that are stable for many hours in cortical slice cultures. *J. neuroscience* **24**, 5216–5229 (2004).
11. Destexhe, A., Rudolph, M. & Paré, D. The high-conductance state of neocortical neurons in vivo. *Nat. reviews neuroscience* **4**, 739–751 (2003).
12. El Boustani, S. *et al.* Network-state modulation of power-law frequency-scaling in visual cortical neurons. *PLoS computational biology* **5**, e1000519 (2009).
13. Milstein, J., Mormann, F., Fried, I. & Koch, C. Neuronal shot noise and brownian 1/f² behavior in the local field potential. *PloS one* **4**, e4338 (2009).
14. Manning, J. R., Jacobs, J., Fried, I. & Kahana, M. J. Broadband shifts in local field potential power spectra are correlated with single-neuron spiking in humans. *J. Neurosci.* **29**, 13613–13620 (2009).
15. Miller, K. J., Sorensen, L. B., Ojemann, J. G. & Den Nijs, M. Power-law scaling in the brain surface electric potential. *PLoS computational biology* **5**, e1000609 (2009).

16. Pettersen, K. H., Lindén, H., Tetzlaff, T. & Einevoll, G. T. Power laws from linear neuronal cable theory: power spectral densities of the soma potential, soma membrane current and single-neuron contribution to the EEG. *PLoS computational biology* **10**, e1003928 (2014).
17. Schreiner, J., Kessler, U., Oedegaard, K. J., Mardal, K.-A. & Olteidal, L. Exploring new EEG parameters in electroconvulsive therapy. *medRxiv* DOI: [10.1101/2021.11.03.21265830](https://doi.org/10.1101/2021.11.03.21265830) (2021). <https://www.medrxiv.org/content/early/2021/11/03/2021.11.03.21265830.full.pdf>.
18. Tung, L. *A Bi-domain model for describing ischemic myocardial dc potentials*. Ph.D. thesis, Massachusetts Institute of Technology (1978).
19. Henriquez, C. S., Muzikant, A. L. & Smoak, C. K. Anisotropy, fiber curvature, and bath loading effects on activation in thin and thick cardiac tissue preparations: Simulations in a three-dimensional bidomain model. *J. cardiovascular electrophysiology* **7**, 424–444 (1996).
20. Pollard, A. E., Hooke, N. & Henriquez, C. S. Cardiac propagation simulation. *Critical reviews biomedical engineering* **20**, 171–210 (1992).
21. Roth, B. J. A comparison of two boundary conditions used with the bidomain model of cardiac tissue. *Annals biomedical engineering* **19**, 669–678 (1991).
22. Sundnes, J. *et al.* *Computing the electrical activity in the heart*, vol. 1 (Springer Science & Business Media, 2007).
23. Rincon, A. L. & Shimoda, S. The inverse problem in electroencephalography using the Bidomain model of electrical activity. *J. neuroscience methods* **274**, 94–105 (2016).
24. Lopez-Rincon, A., Cantu, C., Etcheverry, G., Soto, R. & Shimoda, S. Function based brain modeling and simulation of an ischemic region in post-stroke patients using the Bidomain. *J. Neurosci. Methods* **331**, 108464 (2020).
25. Bai, S., Loo, C., Al Abed, A. & Dokos, S. A computational model of direct brain excitation induced by electroconvulsive therapy: comparison among three conventional electrode placements. *Brain Stimul.* **5**, 408–421 (2012).
26. Hodgkin, A. L. & Huxley, A. F. A quantitative description of membrane current and its application to conduction and excitation in nerve. *The J. physiology* **117**, 500–544 (1952).
27. Næss, S. *et al.* Corrected four-sphere head model for EEG signals. *Front. human neuroscience* **11**, 490 (2017).
28. Lee, W. H. *et al.* Regional electric field induced by electroconvulsive therapy in a realistic finite element head model: influence of white matter anisotropic conductivity. *Neuroimage* **59**, 2110–2123 (2012).
29. Jirsa, V. K., Stacey, W. C., Quilichini, P. P., Ivanov, A. I. & Bernard, C. On the nature of seizure dynamics. *Brain* **137**, 2210–2230 (2014).
30. Spiegler, A., Hansen, E. C., Bernard, C., McIntosh, A. R. & Jirsa, V. K. Selective activation of resting-state networks following focal stimulation in a connectome-based network model of the human brain. *Eneuro* **3** (2016).
31. Fischl, B. *et al.* Whole brain segmentation: automated labeling of neuroanatomical structures in the human brain. *Neuron* **33**, 341–355 (2002).
32. Fischl, B. *et al.* Sequence-independent segmentation of magnetic resonance images. *Neuroimage* **23**, S69–S84 (2004).
33. Valnes, L. & Schreiner, J. SVMTK. <https://github.com/SVMTK/SVMTK>.
34. The CGAL Project. *CGAL User and Reference Manual* (CGAL Editorial Board, 2020), 5.2 edn.
35. Tuch, D. S., Wedeen, V. J., Dale, A. M., George, J. S. & Belliveau, J. W. Conductivity tensor mapping of the human brain using diffusion tensor MRI. *Proc. Natl. Acad. Sci.* **98**, 11697–11701 (2001).
36. Bangera, N. B. *et al.* Experimental validation of the influence of white matter anisotropy on the intracranial EEG forward solution. *J. computational neuroscience* **29**, 371–387 (2010).
37. Morris, C. & Lecar, H. Voltage oscillations in the barnacle giant muscle fiber. *Biophys. journal* **35**, 193–213 (1981).
38. Welch, P. The use of fast fourier transform for the estimation of power spectra: a method based on time averaging over short, modified periodograms. *IEEE Transactions on audio electroacoustics* **15**, 70–73 (1967).
39. Virtanen, P. *et al.* Scipy 1.0: fundamental algorithms for scientific computing in python. *Nat. methods* **17**, 261–272 (2020).
40. Vorwerk, J. *et al.* A guideline for head volume conductor modeling in eeg and meg. *NeuroImage* **100**, 590–607 (2014).
41. Rognes, M. E., Farrell, P. E., Funke, S. W., Hake, J. E. *et al.* cbcbeat: an adjoint-enabled framework for computational cardiac electrophysiology. *J. Open Source Softw.* **2**, 224 (2017).

42. Alnæs, M. *et al.* The FEniCS project version 1.5. *Arch. Numer. Softw.* **3** (2015).
43. Logg, A., Mardal, K.-A. & Wells, G. *Automated solution of differential equations by the finite element method: The FEniCS book*, vol. 84 (Springer Science & Business Media, 2012).
44. He, B. J., Zempel, J. M., Snyder, A. Z. & Raichle, M. E. The temporal structures and functional significance of scale-free brain activity. *Neuron* **66**, 353–369 (2010).
45. Freeman, W. J. & Zhai, J. Simulated power spectral density (PSD) of background electrocorticogram (ECoG). *Cogn. neurodynamics* **3**, 97–103 (2009).
46. Miller, K. J., Sorensen, L. B., Ojemann, J. G. & Nijs, M. d. ECoG observations of power-law scaling in the human cortex. *arXiv preprint arXiv:0712.0846* (2007).
47. Nunez, P. & Srinivasan, R. *Electrical fields of the brain 2nd ed* (New York, NY: Oxford University Press, 2005).
48. Logothetis, N. K., Kayser, C. & Oeltermann, A. In vivo measurement of cortical impedance spectrum in monkeys: implications for signal propagation. *Neuron* **55**, 809–823 (2007).
49. Miceli, S., Ness, T. V., Einevoll, G. T. & Schubert, D. Impedance spectrum in cortical tissue: Implications for propagation of LFP signals on the microscopic level. *Eneuro* **4** (2017).
50. Gomes, J.-M. *et al.* Intracellular impedance measurements reveal non-ohmic properties of the extracellular medium around neurons. *Biophys. journal* **110**, 234–246 (2016).
51. Barbour, B. Analysis of claims that the brain extracellular impedance is high and non-resistive (2017).
52. Bédard, C. & Destexhe, A. Is the extracellular impedance high and non-resistive in cerebral cortex? (2017).
53. Bédard, C. & Destexhe, A. Macroscopic models of local field potentials and the apparent 1/f noise in brain activity. *Biophys. journal* **96**, 2589–2603 (2009).
54. Wei, Y., Ullah, G. & Schiff, S. J. Unification of neuronal spikes, seizures, and spreading depression. *J. Neurosci.* **34**, 11733–11743 (2014).
55. von Bartheld, C. S., Bahney, J. & Herculano-Houzel, S. The search for true numbers of neurons and glial cells in the human brain: a review of 150 years of cell counting. *J. Comp. Neurol.* **524**, 3865–3895 (2016).

7 Acknowledgement

The authors want to thank Leif Oltedal, Ola Skavhaug, and Aslak Tveito for stimulating discussions, Kyrre Emblem and Siri Fløgstad for making the MRI data available, and Miroslav Kuchta for assistance with creating Figure 4b. JS acknowledges support from the Research Council of Norway, grant 273077. KAM acknowledges support from the Research Council of Norway, grant 300305 and 301013. The simulations were performed on resources provided by UNINETT Sigma2 - the National Infrastructure for High Performance Computing and Data Storage in Norway

8 Author Contributions

Both authors conceived of the study. JS implemented the simulators, conducted experiments and made the figures. Both authors discussed and analysed the results, and wrote and edited the manuscript.

9 Competing Interests

The authors declare no competing interests.